

ZHANG Yue, HUANG Yun-hua, HE Jian,  
DAI Ying, ZHANG Xiao-mei,  
LIU Juan, LIAO Qing-Liang

## Quasi One-dimensional ZnO Nanostructures Fabricated without Catalyst at Lower Temperature

© Higher Education Press and Springer-Verlag 2006

**Abstract** One- or quasi one-dimensional zinc oxide nanostructures possess plenty of morphologies. Only by controlling the gas flow rates, and partial pressures of argon, oxygen and zinc vapor, can various types of high-quality ZnO nanomaterials (such as wires, belts, arrays, saws or combs, tetraleg rods, nails, and pins) be synthesized through pure zinc powder evaporation without a catalyst at the temperature range of 600–700°C. In this study, deposited nanostructures were characterized by means of scanning electron microscopy, X-ray diffraction and high-resolution transmission electron microscopy. The authors propose and discuss the growth mechanisms of various ZnO. In addition, properties of room temperature photoluminescence and field emission of several typical ZnO nanostructures are measured and investigated.

**Keywords** zinc oxide, nanostructure, growth mechanism, photoluminescence, field emission property

**PACS numbers** 61.46.-w, 78.67.-n, 79.70.+q, 81.07.-b

### 1 Introduction

Zinc oxide has a hexagonal structure, lattice constants  $a=0.324\text{--}0.326$  nm and  $c=0.513\text{--}0.543$  nm, a wide band-gap of 3.37 eV and a large exciton binding energy of 60 MeV at room temperature [1–3]. This one-dimensional (1D) or quasi 1D zinc oxide nanomaterials are promising materials for applications in blue light-emitting diodes (LEDs), field-effect transistors (FET), ultraviolet laser diodes (LD), sensors, acousto-electrical devices, and detectors. ZnO nanostructures have attracted considerable attention due to numerous fundamental studies as well as applica-

tions in one-dimensional nanodevices and other functional materials. In addition to nanowires, nanobelts, tetrapod-like nanorods and nanotubes [4–9], other interesting nanostructures such as nanocombs, toothed nanobelts, nanopropellers, nanosprings and nanorings have also been synthesized [9–14].

Conventionally, according to growth mechanism, the main fabrication methods of 1D ZnO nanostructures are vapor–solid (VS) growth, vapor–liquid–solid (VLS) growth and polar-surface dominated growth [14–16]. VLS growth requires the involvement of a liquid-forming (or so-called catalysts) additive [16,17]. Catalysts such as copper, gold, cobalt or other transition metal nanoparticles/film can often be used. In this method, the usual synthesis temperature is in the range of 850–950°C [2,3,16–19], and the lowest preparation temperature for ZnO nanowires was reported to be 450°C (NiO catalyzed) [20]. The synthesis temperature for ZnO nanostructures by VS growth is from ~850°C (Zn powder evaporation) to ~1400°C (zinc oxide powder evaporation) [6,15,21–24]. The temperature by VLS growth is much lower, but catalysts in the nanomaterials may affect purity and, possibly, properties.

In this paper, we report some novel quasi 1D ZnO nanostructures, such as wires, belts, arrays, saws or combs, tetraleg rods, nails, pins, etc., fabricated by an improved method. Such nanostructures were prepared onto a silicon substrate by metal zinc powder evaporation and deposition without a catalyst at a lower temperature. The growth mechanisms of various ZnO were proposed and discussed. In addition, properties of room temperature photoluminescence (PL) and field emission (FE) of several typical ZnO nanostructures were measured and investigated. Other investigations in our laboratory can be found in correlative literatures.

### 2 Experimental

The ZnO nanostructures were fabricated by the following procedure. The silicon substrate (15 mm×15 mm) was placed facedown on an aluminum ceramic boat loaded with metal zinc powder (99.9%) with a thickness of 1–3 mm. The vertical distance between the zinc source and the

ZHANG Yue (✉), HUANG Yun-hua, HE Jian,  
DAI Ying, ZHANG Xiao-mei,  
LIU Juan, LIAO Qing-Liang  
Department of Materials Physics,  
University of Science and Technology Beijing,  
Beijing 100083, China  
E-mail: Yuezhang@ustb.edu.cn

substrate was about 5–8 mm. The boat [10 mm×10 mm×100 mm (length)] was inserted into a quartz tube (inside diameter, 30 mm; length, 1000 mm) of a tubular furnace under a constant flow of argon and oxygen. The total flow rate was 200–300 standard cubic centimeters per minute (sccm), and the fraction of oxygen was 1%–10% depending on the different conditions. Gases were fed and mixed by a Y-shaped tube and controlled by mass flowmeter. The quartz tube was heated up to 600–700°C for 20–40 min. After evaporation, the exposed substrate surface (15 mm×10 mm) showed full of white wax or fluffy-like materials. No catalyst was utilized in all the deposition processes.

The deposited products were characterized by scanning electron microscopy (SEM; Cambridge S360), field emission scanning electron microscopy (FE-SEM; JEOL-6700F), X-ray diffraction (XRD; Rigaku DMAX-RB) and high-resolution transmission electron microscopy (HRTEM; JEOL-2010). The PL spectrum was measured via a Hitachi 4500-type Vis–UV spectrophotometer with a Xe lamp as the excitation light source at room temperature. Field emission experiments were carried out with a Keithley 2410 picoammeter.

### 3 Results and discussion

#### 3.1 Morphologies and structures

ZnO nanostructures exhibited plentiful morphology through various synthesis routes, of which thermal evaporation is

typical and efficient. Through pure zinc powder evaporation without catalyst, the novel and simple method is important and promising due to a mass of morphologies and high purity of products, lower synthesis temperature, etc.

##### 3.1.1 Nanowires, nanobelts and nanoarrays

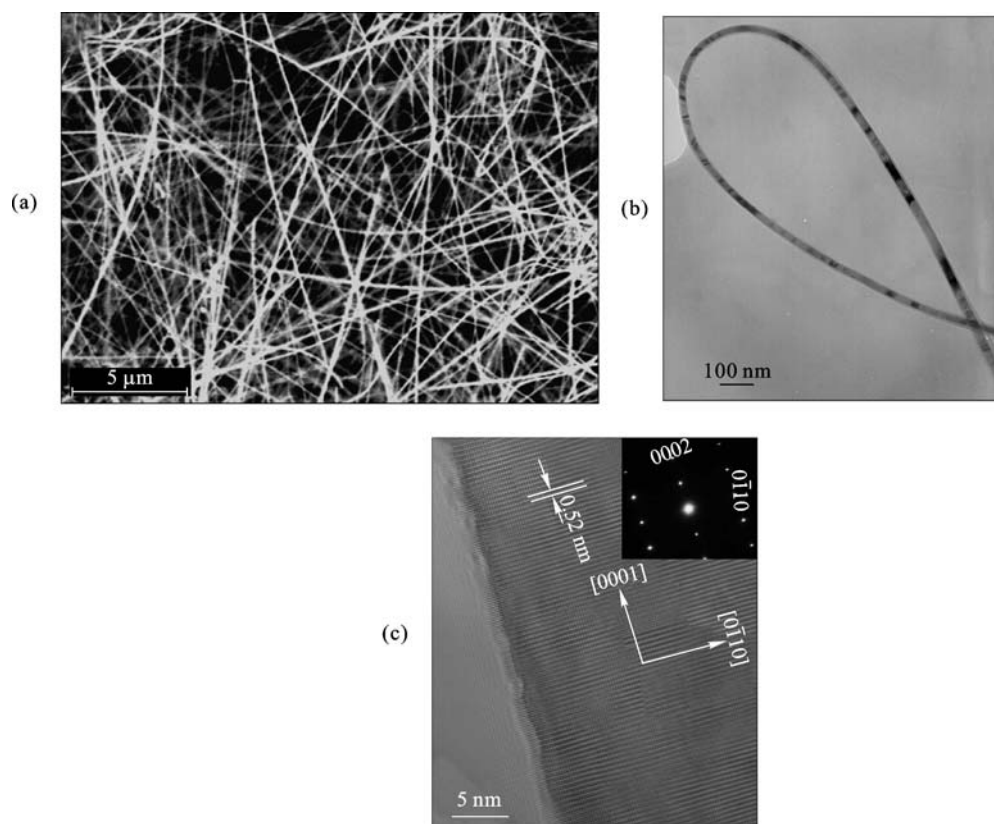
ZnO nanowires, nanobelts and nanoarrays are the most typical nanostructures. Figures 1, 2, 3 show the SEM and TEM images of such synthesized nanostructures, respectively.

In the experimental process, ZnO nanowires (Fig. 1) grew at a total flow rate of ~300 sccm, oxygen partial pressure of ~1%, and 650°C; the nanobelts (Fig. 2) grew at ~280 sccm, O<sub>2</sub> partial pressures of 1%–1.5% and 650 °C; the nanoarrays (Fig. 3a) synthesized at 650°C and ~280 sccm flow rate, ~3% O<sub>2</sub>, and arrays (Fig. 3b) were obtained at 700°C, ~250 sccm, ~3% O<sub>2</sub>.

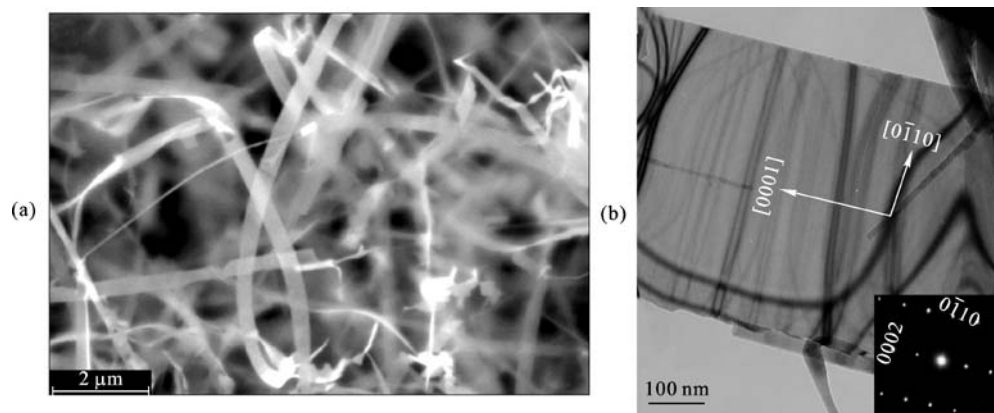
Figures 1(a) and (b) shows that the diameter of ZnO nanowires is about several tens of nanometers and the length is up to several tens of microns; it also reveals that the wires are very flexible. The HRTEM image [Fig. 1(c)] shows the smooth surface and the growth direction. The growth accords the normal direction as [0001].

Figure 2 shows that the typical width of belts is from 400 nm to 900 nm, the thickness is from 10 nm to 50 nm, while the length runs to several tens of microns. In Fig. 2(b) and the inset, the lengthways growth direction is [0001],

**Fig. 1** Images of ZnO nanowires. (a) SEM image, (b) TEM image, (c) HRTEM image and SAED pattern



**Fig. 2** Images of ZnO nanobelts. (a) SEM image, (b) TEM image and diffraction pattern



that of transverse is  $[0\bar{1}10]$ . The images also present the almost perfect surfaces.

Typically fabricated nanoarrays exhibit two kinds of morphologies (as seen in Fig. 3). SEM images show that the nanoarrays in Fig. 3(a) include thicker roots (with diameters of 400–600 nm), thinner trunks (with diameters of 60–100 nm and lengths of up to several microns) and sharp tips. The arrays in Fig. 3(b) are hexagonal prism with ‘diameters’ of 400–600 nm and flat tops. These different geometries can markedly influence the FE property (which will be discussed later).

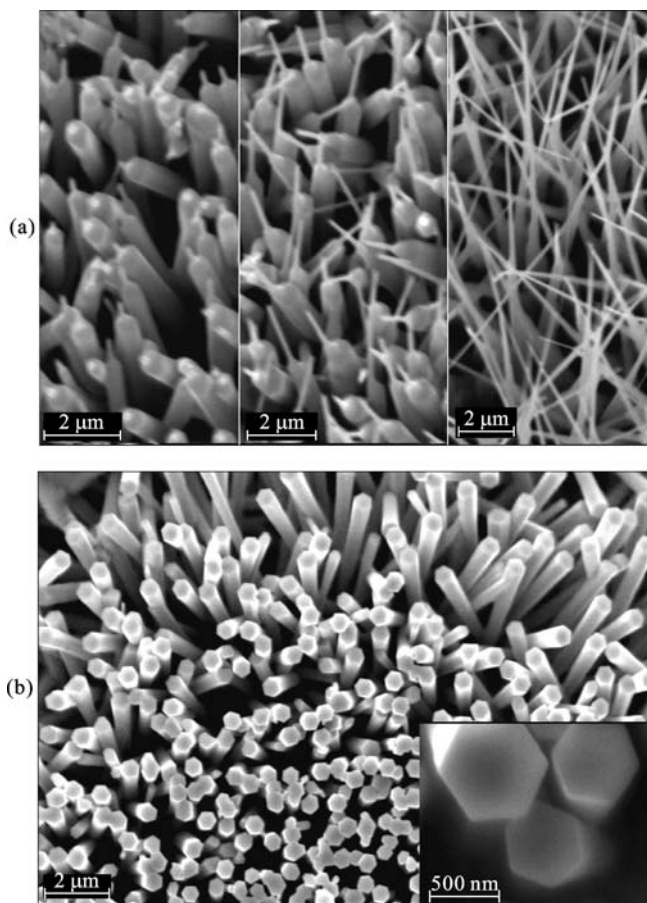


**Fig. 3** SEM images of ZnO nanoarrays

Figure 3(a) also reveals the growth process of ZnO nanoarrays. Each panel (from left to right) in the figure corresponds to the reaction time of 10, 15 and 20 min, respectively. It can be observed that the thicker roots form at first. After a while, the roots stop growing and the trunks begin to grow until the reaction is completed.

### 3.1.2 Toothed nanostructures

Toothed nanostructures are typical quasi 1D ZnO nano-materials. Figure 4 shows the SEM images of four types of ZnO toothed nanostructures: nanosaws I type, nanosaws II type, nanocombs and double-sided nanocombs.

The fabrication conditions are shown in Fig. 4. In this paper, the long and flexible toothed nanostructures are named nanosaws, while the shorter and rigid ones are called nanocombs. The backbones of nanosaws I, as shown in Fig. 4(a), are smooth, while those of nanosaws II, as shown in Fig. 4(b), are uneven as a washboard.

Figures 4(a)–(c) show that the typical width of the backbones of toothed nanostructures is from 400 nm to 900 nm, the thickness is from 50 nm to 100 nm, while the length is over a hundred microns (saws) or up to several tens of microns (combs). The teeth have diameters ranging from 50 nm to 100 nm, and the lengths are about hundreds of nanometers to several microns. The teeth of the nanostructures exhibit regular diameter, length and spacing.

Figure 5 shows the HRTEM images and the selected area electron diffraction (SAED) pattern of nanosaws I. SAED pattern and HRTEM image reveal that the ZnO toothed nanostructures are structurally uniform and single crystalline. In zinc oxide crystal with hexagonal structure,  $[0001]$ ,  $[2\bar{1}10]$ , and  $[0\bar{1}10]$  are the preferential growth directions. The images also suggest that tooth growth occurs along the  $[0001]$  direction and the backbone along  $[0\bar{1}10]$ .

Figure 4(d) and Fig. 6 show that the teeth of double-sided nanocombs also exhibit regular diameter, length and spacing. Descending gradually along the direction of main stems’ growth, teeth length ranges from 2 μm to hundreds of nanometers. Changes in the width of the main stems show the same trend. The two insets of TEM image [Fig. 6(a)] reveal that the diameter of teeth in the central

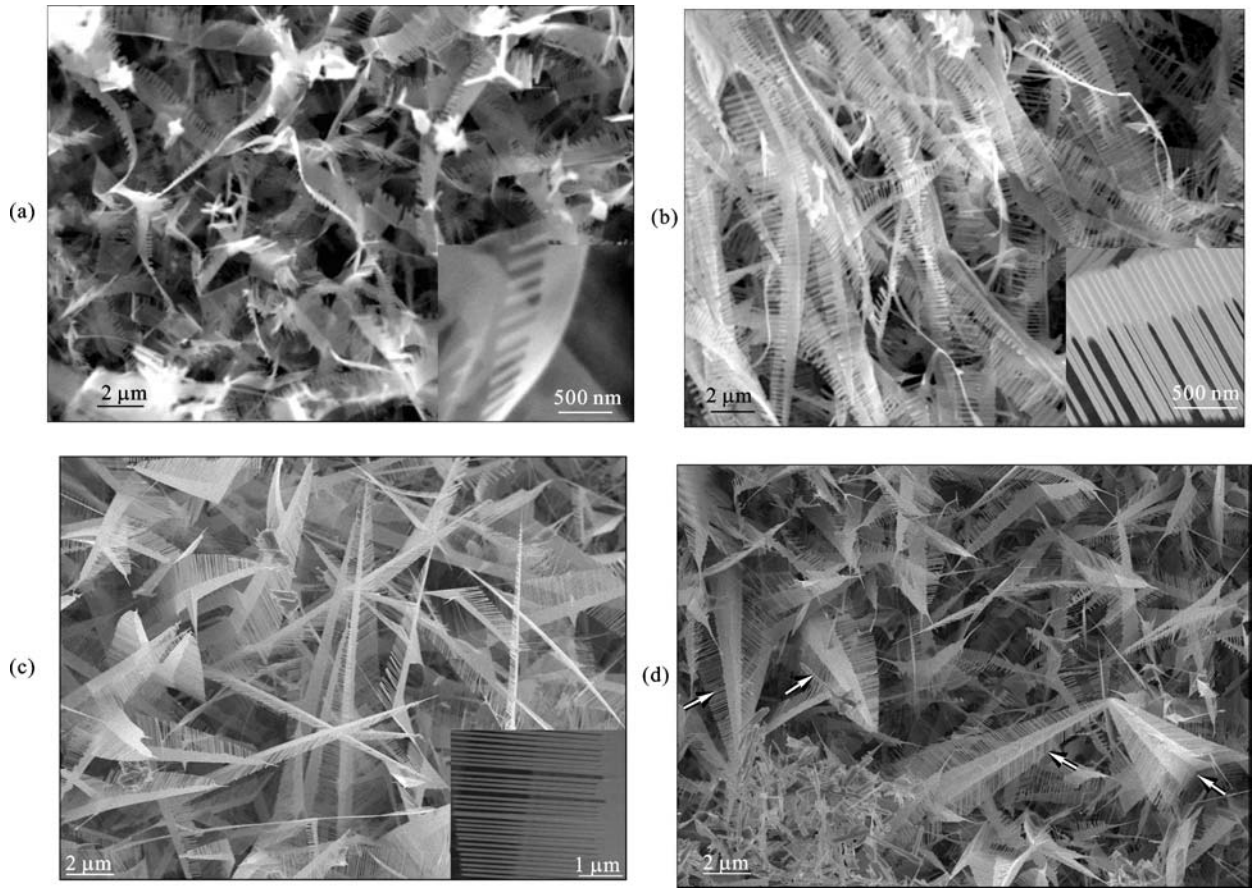


**Fig. 4** SEM images of ZnO toothed nanostructures. (a) Nanosaws I [Ar+O<sub>2</sub> (~2%)=200–230 sccm, 600°C], (b) nanosaws II [Ar+O<sub>2</sub> (3%–5%)=220–260 sccm, 600°C], (c) nanocombs [Ar+O<sub>2</sub> (2%–3%)=~250 sccm, 650°C], (d) double-sided combs [Ar+O<sub>2</sub> (2%)=250 sccm, 650°C]

section is about 50 nm, and the maximum diameter of teeth in the tail section is about 100 nm. The insets also revealed the contrast in images of different nano areas, i.e., the different thickness of each part of the combs. The central line along the stem (as shown in the right-upper inset)

presents as a clear edge, and the teeth in each side are perpendicular to the edge. The two sides of the double-sided comb exhibit mirror symmetry. Teeth of each side grew along  $\langle 0001 \rangle$  and stems along  $\langle 0\bar{1}10 \rangle$ . This will be discussed in more detail later.

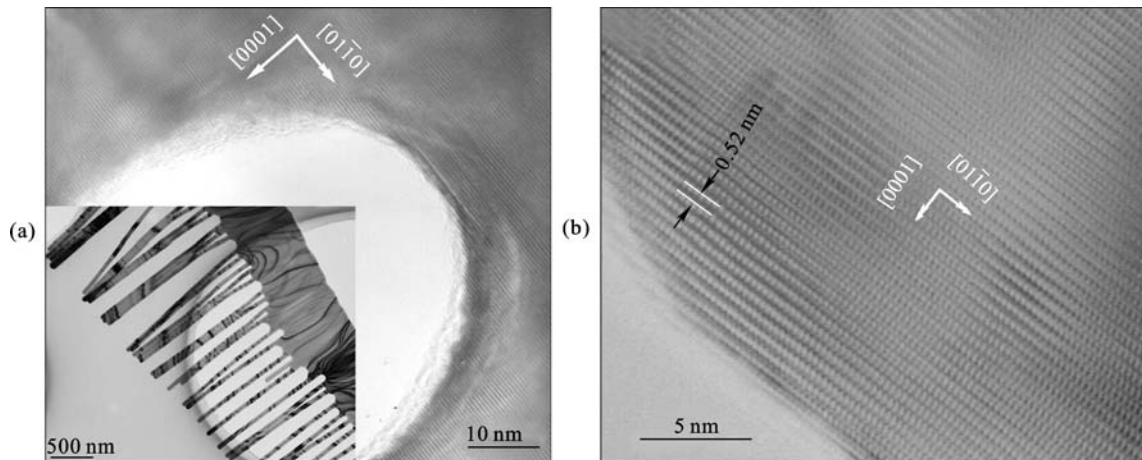


**Fig. 5** TEM and HRTEM images of ZnO nanosaws I type. (a) Image of the joint of the tooth and backbone, (b) image of the tip of the tooth

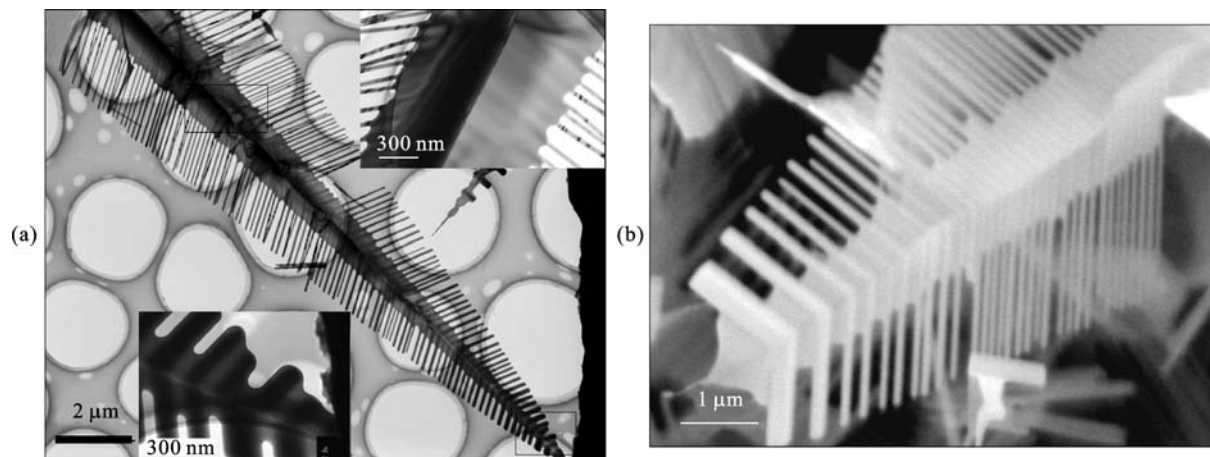


**Fig. 6** TEM and FE-SEM images of double-sided ZnO nanocombs. (a) TEM images, (b) FE-SEM image

### 3.1.3 Tetraleg nanorods

Tetraleg ZnO (T-ZnO) nanorods are another typical quasi 1D ZnO nanostructures. As a variable element in fabrication conditions, the nanoscale T-ZnO products exhibit several types of morphologies with different shapes and sizes of the legs. Leg shapes include thin needle (type I), columnar needle (type II), hexagonal (type III), nail-like (type IV), etc. Figure 7 shows the images of T-ZnO and the

synthesis parameters are included in the caption. The images reveal that the leg length of T-ZnO nanorods is 2–10  $\mu\text{m}$  and the diameter is in the range of several tens to several hundreds nanometers.

Dai et al. [22] investigated T-ZnO via octa-twin nucleus models [25] and TEM and HRTEM observation. According to the crystal vapor nucleation mechanism, ZnO nuclei formed in the alumina crucible are homogeneous nucleation in gas phase. Firstly, octa-twins nuclei form in an

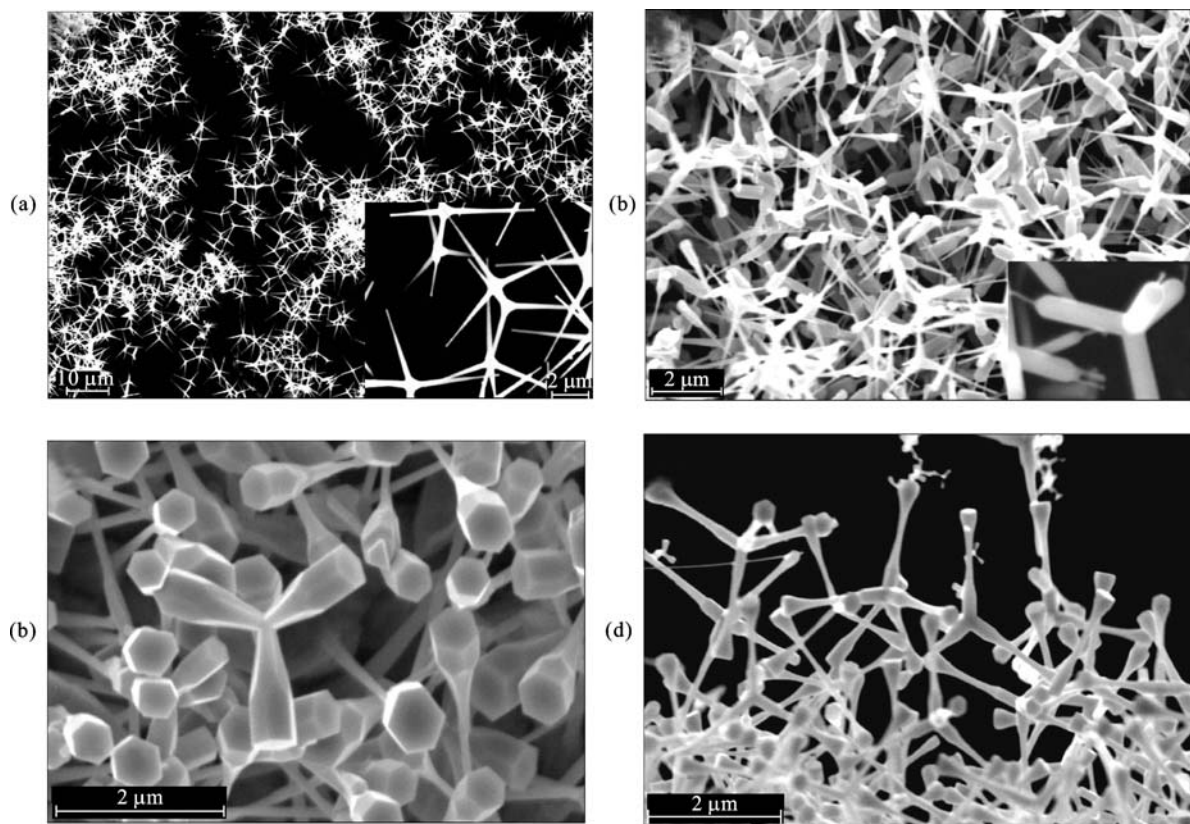


**Fig. 7** SEM images of T-ZnO nanorods. (a) type I T-ZnO with thin needle legs (fabricated at 600°C and ~330 sccm flow rate, ~3% O<sub>2</sub>), (b) type II T-ZnO with columnar-needle legs (650°C, ~300 sccm, ~5% O<sub>2</sub>), (c) type III T-ZnO with hexagonal legs (750°C, ~280 sccm, ~6% O<sub>2</sub>), (d) type IV T-ZnO with nail-like legs (650°C, ~270 sccm, ~7% O<sub>2</sub>)

atmosphere containing oxygen. The octa-twin nuclei comprise eight tetrahedral crystals, each consisting of three  $\{11\bar{2}2\}$  pyramidal faces and one  $\{0001\}$  basal face. The eight tetrahedral crystals are connected together by making the pyramidal faces contact one another to form an octahedron. The surfaces of the octo-twin are composed of basal planes. An important additional condition is that every twin is of the inversion type, i.e., the polarities of the twinned crystals are not mirror-symmetric with respect to the contact plane, but rather antisymmetric. Thus, the eight basal surfaces of the octa-twin are alternately the plus surface (0001) and the minus surface (000 $\bar{1}$ ), as illustrated in Fig. 8(a). In a small nucleus, a large contribution of the surface energy to the total energy prevents the octa-twin from the crack formation. The crystal growth results from the oriented adsorption of vapor-nucleating species on certain single crystalline nucleus surface with relatively high surface energy. Due to the crystallographic polarity of ZnO crystal, legs grow preferentially perpendicular to the four plus (0001) surfaces. A preferential growth in the  $+c$  direction has already been confirmed for ZnO crystal.

A TEM image of T-ZnO nanorod is shown in Fig. 8(b). There exist four boundaries in the central part. The other two interfaces are found in both left and right legs (marked by arrows), and the upper and lower legs are single crystals. Figure 8(c), which shows the corresponding HRTEM image of the central part in Fig. 8(b), reveals the structure of the boundaries between the element crystals. The interfaces are sharp and show no amorphous layer. Four crystals twin each other, and thus four twinning boundaries form. These twins are smoothly conjugated on the boundaries and united in a coherent relationship, indicating little lattice distortion near the boundary.

### 3.1.4 Nanonails and nanopins

Figures 9(a) and (b) show two types of ZnO nanonails. Nanonails with concave arc neck [Fig. 9(a)], whose length

ranged from 2  $\mu\text{m}$  to 3  $\mu\text{m}$ , were prepared under 200 sccm of Ar–O<sub>2</sub> (~1.5%) at 600°C. The caps show a perfect hexagonal symmetry with a diameter of about 900 nm, while the diameter of trunks is about 100 nm. The nanonails with bevel neck [Fig. 9(b)], with length exceeding 5  $\mu\text{m}$ , were prepared under 200 sccm of Ar–O<sub>2</sub> (~1%) at 650°C. The diameter of trunks is about 200–300 nm, while that of hexagonal caps is about 1  $\mu\text{m}$ . Inset in Fig. 9(b) shows that the growth direction is the preferential direction [0001].

The ZnO nanopins [Fig. 9(c)] were synthesized at 200 sccm of Ar–O<sub>2</sub> (~3%) at 700°C. The diameter of a single nanopin's shaft is about 100 to 300 nm, while the length is around 5  $\mu\text{m}$ . The growth of nanopins is discussed in Section 3.2.

### 3.1.5 Other nanostructures

Aside from typical and controlled-shape ZnO nanomaterials mentioned above, other interesting and useful structures have been prepared under specific conditions. Although the fabrication parameters were not mastered, investigation results are promising. Novel structural features, such as coherency or coupling devices, medicine nanocapsules, cluster effects devices, and crossbar junction arrays, are helpful if one wants to build desired systems in nanoscale.

Figure 10 shows several novel ZnO nanostructures obtained occasionally. Further work is needed to seek for synthesis methods to control shape and potential applications for such nanostructures.

## 3.2 Growth mechanisms

The typical growth mechanisms of ZnO nanomaterials include VS, VLS and polar growth mechanism. In our fabrications, the growths involved VS, polar mechanism and a new mechanism, which we introduce for the first time.

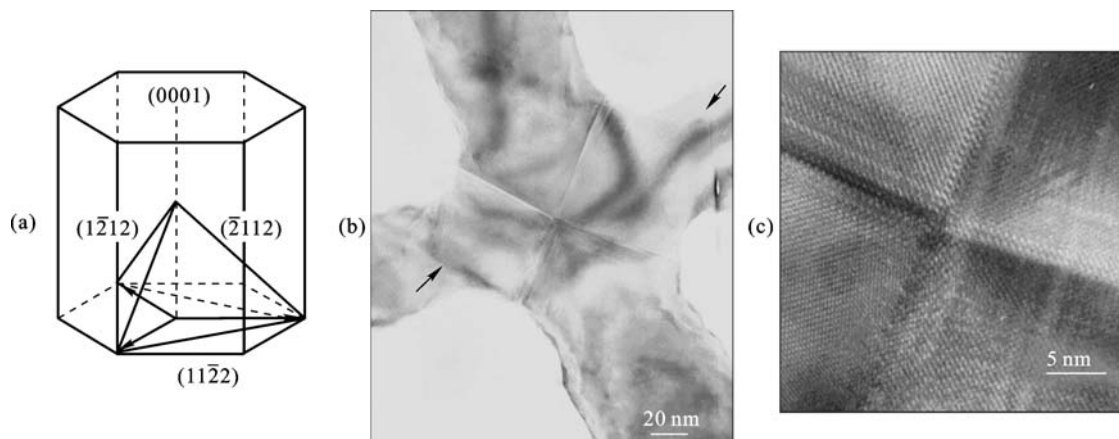


**Fig. 8** Octa-twin nucleus models and TEM images of a T-ZnO nanorod. (a) Octa-twin composed of eight pyramidal inversion-twin crystals, (b) TEM image, (c) HRTEM image

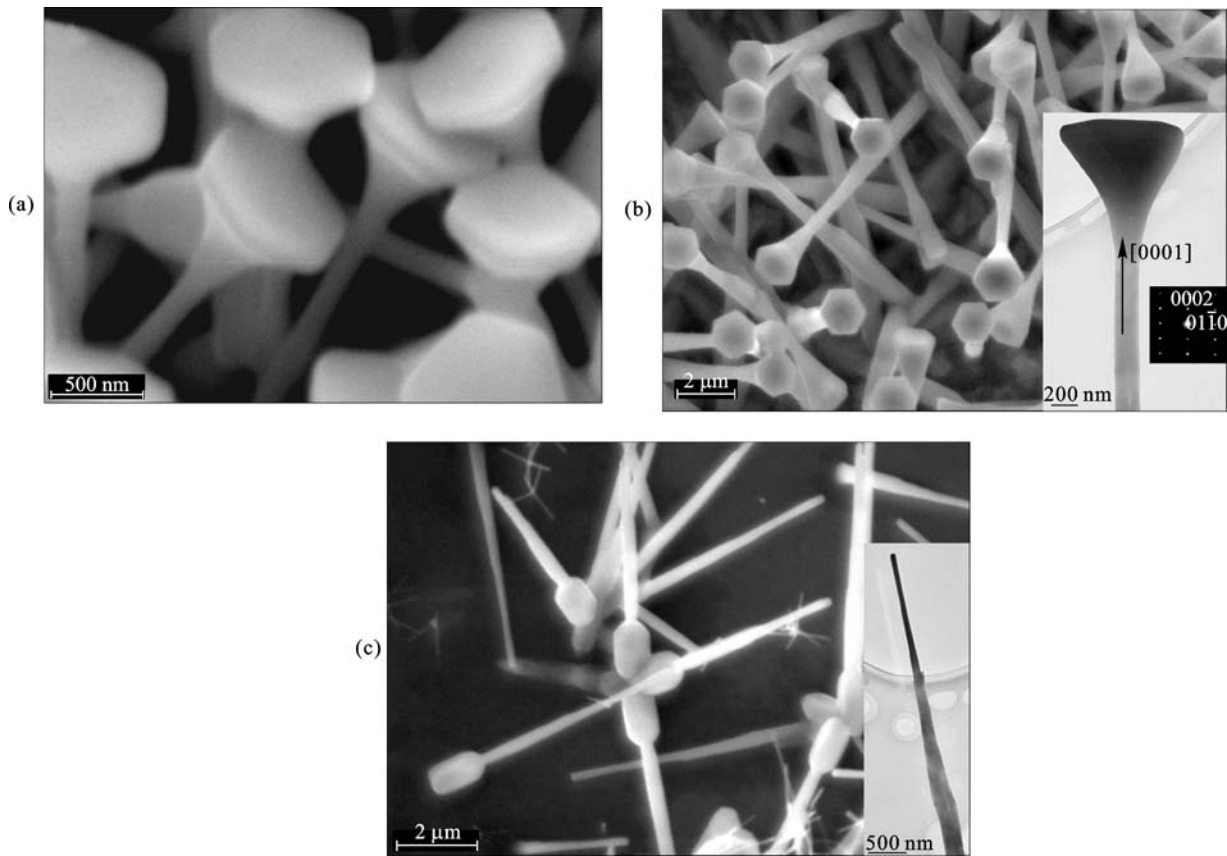


**Fig. 9** Images of ZnO nanonails and nanopins. (a) nanonails with concave arc neck, (b) nanonails with bevel neck, (c) nanopins

### 3.2.1 VS growth

Take, for example, ZnO nanosaws I type [Figs. 4(a) and 5]. Figure 11 shows the XRD spectra and the indexing of nanosaws I. XRD measurement shows that all the deposited materials on the silicon substrate are pure ZnO with a wurtzite structure. No diffraction peaks from Zn or other impurities were found in the samples.

In contrast with VS growth, VLS growth requires the presence of a liquid. The presence of solidified spherical droplets at the tips of nanowires or others are commonly considered to be evidence of the VLS mechanism [16,17]. The growth process can be divided into two stages: the nucleation and growth of eutectic alloy droplets and the growth of nanowires through the liquid droplets due to supersaturation. At the initial nucleation stage, Zn vapor might condense. The geometry of the nanowire suggests that the growth front develops in the liquid state during growth, which is favorable, and serves as the stable site for the rapid stacking of incoming atoms. The growth front experienced a rapid oxidation after the temperature dropped and the nanowire was exposed to an oxygen atmosphere [15]. In contrast, no catalyst is utilized and no solidified droplet is found at the tip of any nanostructure when the growth is governed by a VS process. Such nanomaterials can be formed by oxidation of evaporated zinc vapor in gas phase [6]. In our process, some metallic zinc was in its vapor state. The gaseous zinc diffused and

was immediately oxidized in an oxygen environment. The oxidation reaction at our processing temperature is as follows:  $2 \text{Zn(g)} + \text{O}_2 = 2 \text{ZnO(s)}$ . The process of initial nucleation includes diffusion, collision of atoms and reaction between the vapor molecules (including vapor Zn and  $\text{O}_2$ ). When supersaturation increases to a level at which nuclei formed, the produced ZnO nuclei grow to sizes larger than the critical size. The ZnO nuclei formed in the alumina crucible are homogeneous as carried by the gas phase. Investigations through HRTEM [Fig. 5(b)] and XRD (Fig. 11) indicated that nothing except the ZnO crystal occurred at the tip of tooth or around the structures, i.e., the growth of the fabricated ZnO nanocombs is controlled by VS mechanism.

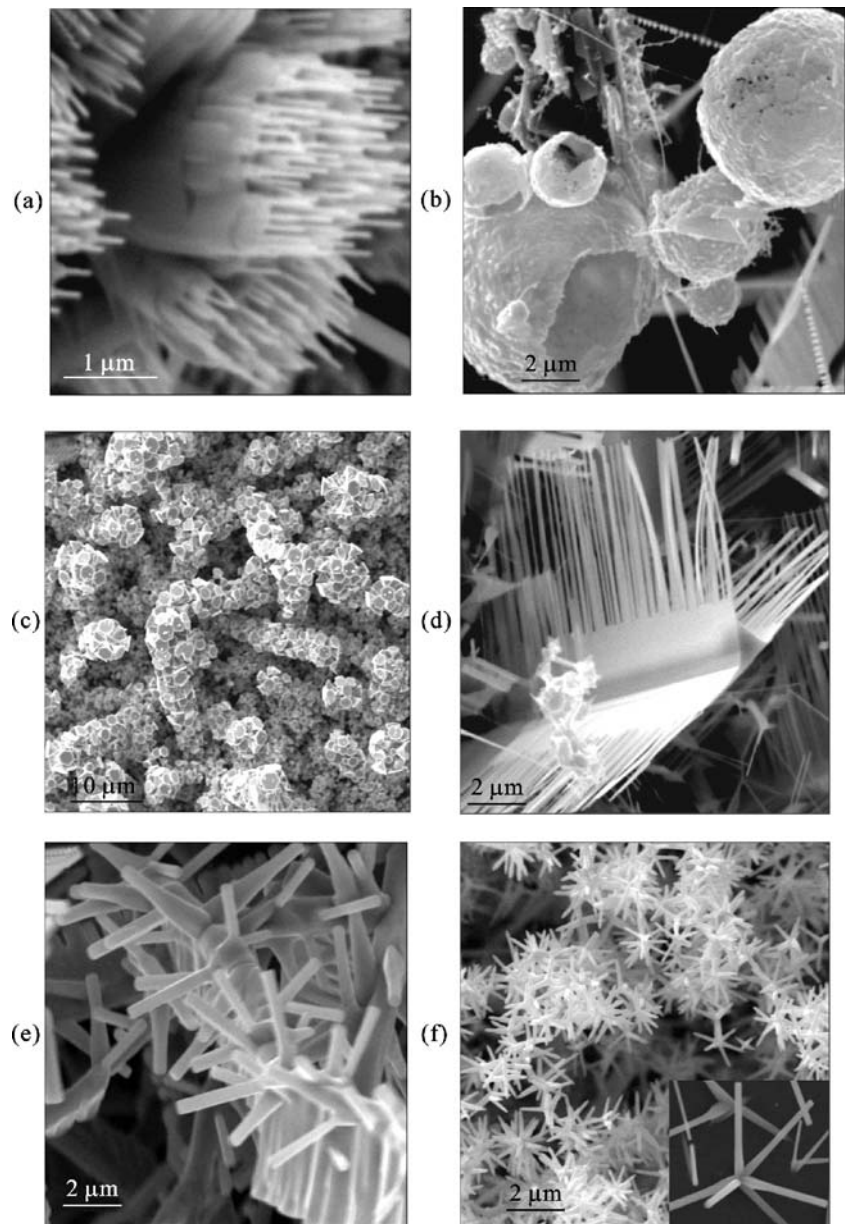
In the same way, it can be confirmed that the growth of other ZnO nanostructures synthesized through the same route is controlled by VS mechanism.

It should be noted that the VS mechanism exists in the growth of ZnO nanosaws I, and other cases do not indicate to exclude other mechanism except VLS mechanism.

### 3.2.2 Polar-surface dominated growth

Double-sided nanocombs [Fig. 4(d)] were investigated as follows. HRTEM and selected area electronic diffraction (SAED) analysis were carried out in the vicinity of the central edge. Figure 12(a) shows the HRTEM image of

**Fig. 10** Some novel ZnO nanostructures



double sides close to the edge. The image reveals sequential and defect-free lattice on each side. Lattice stripes distribute symmetrically and form a pair of twins. The moiré fringe patterns occur near the twin boundary in Fig. 12(a). Because the twin plane is not strictly parallel to the incidence of electron beam and two crystals have differences in orientation, the patterns are produced as a result of overlapping and coherent effect in the area.

The twins of bicrystalline ZnO nanocomb were confirmed by SAED. Two sets of patterns with diffraction zone axis were obtained by tilting the sample. As shown in Fig. 12(a), lattice planes with letters L and R indicate the left and the right indices of the twins, respectively. These patterns exhibit wurtzite structure with higher indices and the zone axis direction of  $[\bar{2}11]$ .

To characterize the structure of the obtained bicrystalline ZnO nanocombs in detail and to confirm the growth directions of each part, an area of the stem further from the edge was selected for SAED analysis. Figure 12(b) shows the TEM image and the relevant diffraction patterns. Results indicate that the stem grew along  $\langle 0\bar{1}10 \rangle$ , while the teeth, which are perpendicular to the twin boundary, grew along  $\langle 0001 \rangle$ . The growth direction accords with that of single crystal ZnO nanocombs reported previously [11,26]. In fact, the SAED patterns from different areas of each side of bicrystalline combs revealed that all of the teeth grew along the  $c$ -axis.

Figure 12(c) shows the HRTEM images of the joint between stem and teeth. The images reveal that any grain boundaries or discontinuous lattice fringes do not exist in the joints, each side of bicrystalline comb is structurally

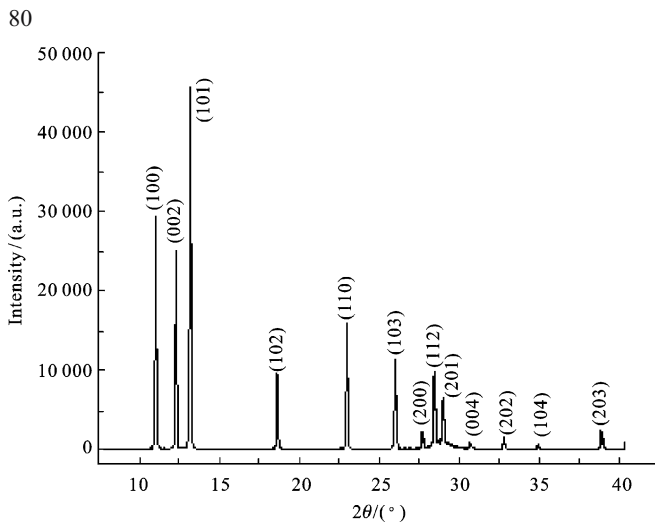


**Fig. 11** XRD pattern of ZnO nanosaws I with a wurtzite structure and cell constants  $a=0.324\ 2\ \text{nm}$  and  $c=0.519\ 4\ \text{nm}$

uniform and single crystalline, and defects only exist at twin boundary. The electronic diffraction patterns in the inset suggest that the crystallographic zone axis is  $[2\bar{1}10]$ .

SAED patterns from all selected areas, including stem and teeth, did not change while the sample was not tilted. Spacing between  $(0\bar{1}\bar{1}0)$  planes measured through Fourier-filtered image equals  $0.28\ \text{nm}$ , and the value accords with the wurtzite structure. It can be confirmed by the present course that teeth grew along  $\langle 0001 \rangle$  and stems along  $\langle 0\bar{1}\bar{1}0 \rangle$ . This is identical with the results outlined above.

According to crystal growth, the stem axis usually accords strictly with  $c$ -axis, which is easy to comprehend by means of the features of ZnO hexagonal structure and preferential growth direction determined by the plane with the lowest formation energy. In contrast with this, teeth of ZnO nanocombs grow along  $\langle 0001 \rangle$ , and stem along  $\langle 0\bar{1}\bar{1}0 \rangle$  or  $\langle 2\bar{1}\bar{1}0 \rangle$ . Wang et al. [26] brought forward the polar-surface dominated growth mechanism to explain such a process. Through convergent beam electron diffraction analysis and theoretical calculation, Wang and co-workers confirmed that the stems of ZnO nanocombs possess polar surfaces, i.e., the  $(0001)$  and  $(000\bar{1})$  surfaces are terminated with Zn positively charged and O negatively

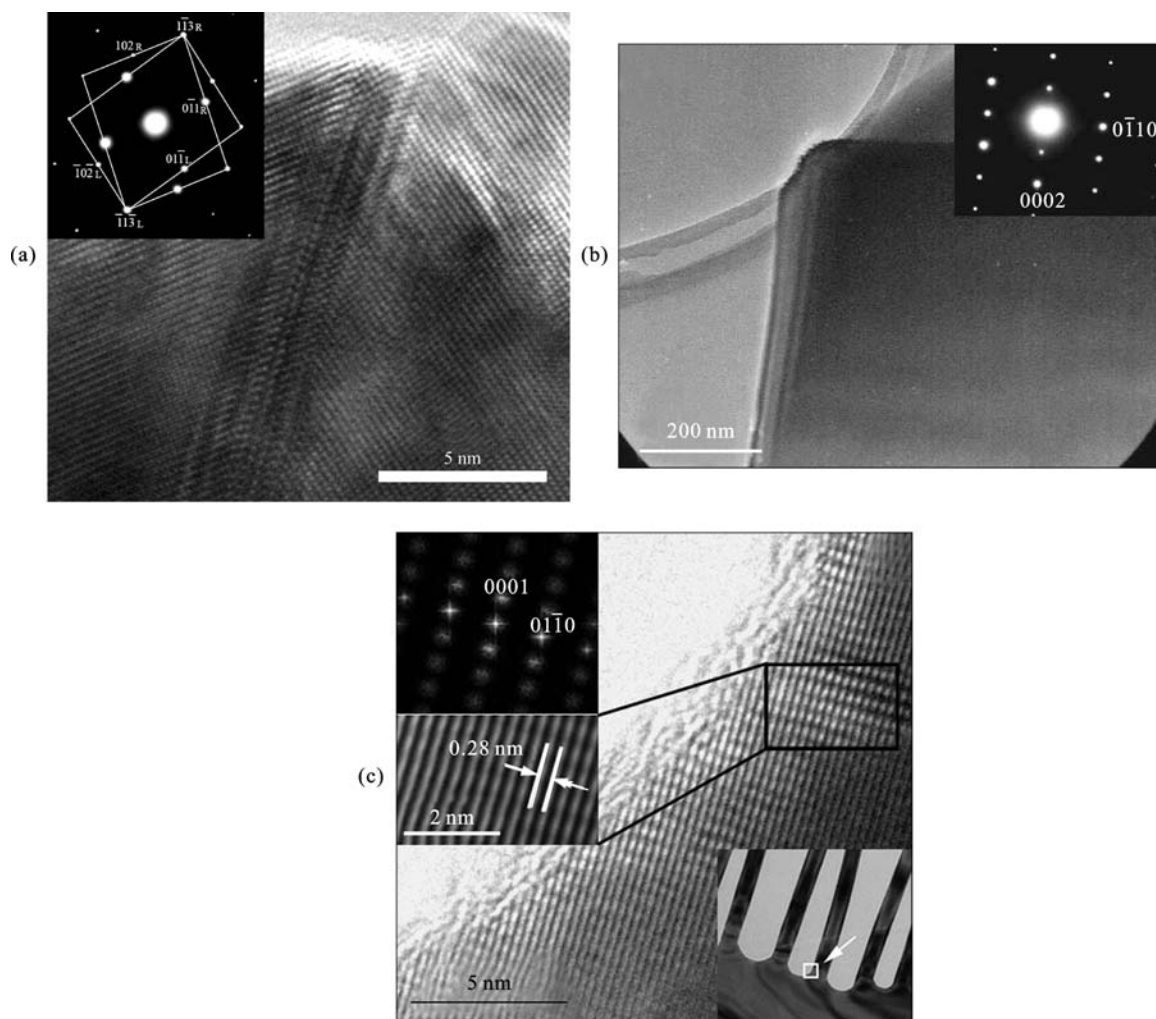


**Fig. 12** TEM images of double-sided nanocombs. (a) HRTEM image of double sides close to the edge, (b) TEM image of the stem further from the edge, (c) HRTEM images of the joint between stem and teeth

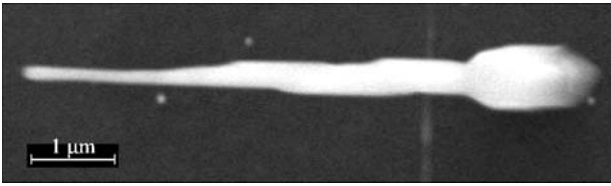


**Fig. 13** Surface of nanopins with screw steps

charged. Comb-like 1D nanoarrays are grown from the (0001)-Zn surface, suggested to be a self-catalyzed process due to the enrichment of Zn at the growth front. The chemically inactive (000 $\bar{1}$ ) surface typically does not initiate any growth; therefore, ZnO nanocombs grow one-sided nanoteeth in most cases when the catalyst is free. Bicrystalline nanocombs with symmetrical, double-sided hierarchical nanostructures synthesized in our experiments were obtained for the first time. Investigations revealed that teeth of each side of bicrystalline combs grow along (0001). According to polar-surface dominated growth mechanism, each side of the combs is sure to grow from the (0001)-Zn surface and through self-catalyzed process due to the enrichment of Zn at the growth front. Such bicrystalline nanocombs are caused by twins that change

crystal orientation and form symmetrical structures. Thus, each side of the structures could present Zn-terminated (0001) surface growth. The synthesized bicrystalline nanocombs are new ZnO structures which are feasible to be explained by polar-surface dominated mechanism. In other words, the growth of bicrystalline ZnO nanocombs brought direct evidence to the polar-surface dominated growth mechanism of the ZnO nanomaterials.

### 3.2.3 Screw dislocation growth

Conventionally, screw dislocation growth put forward by Burton, Cabrera and Frank (BCF) is one of the credible models for the growth of crystal whisker. Some researchers confirmed the dislocation and growth of crystals through HRTEM micrograph analysis [27]. Image of nanopins in Fig. 13 [identical with pins in Fig. 9(c)] exhibits clear screw steps on the surface. The steps are wondrously similar to spirals on micron-scaled carbon whiskers [28]. More credible evidence for the screw dislocations are provided by HRTEM observation. Figure 14 shows the screw dislocations in the tooth of nanosaws I [Fig. 4(a)]. HRTEM images reveal that there are numerous screw dislocations in the tooth of ZnO toothed nanostructures. Arrowheads in

**Fig. 14** Screw dislocations in a tooth of ZnO nanosaws. (a) HRTEM image and SAED pattern of a tooth of a ZnO nanosaw (*arrowheads*, some positions of dislocations; *rectangles*, areas magnified in latter figures), (b) screw dislocations [higher magnification of “b” area in (a)], (c) screw dislocations and growth steps [higher magnification of “c” area in (a); *white arrowheads* indicate some positions of dislocations]

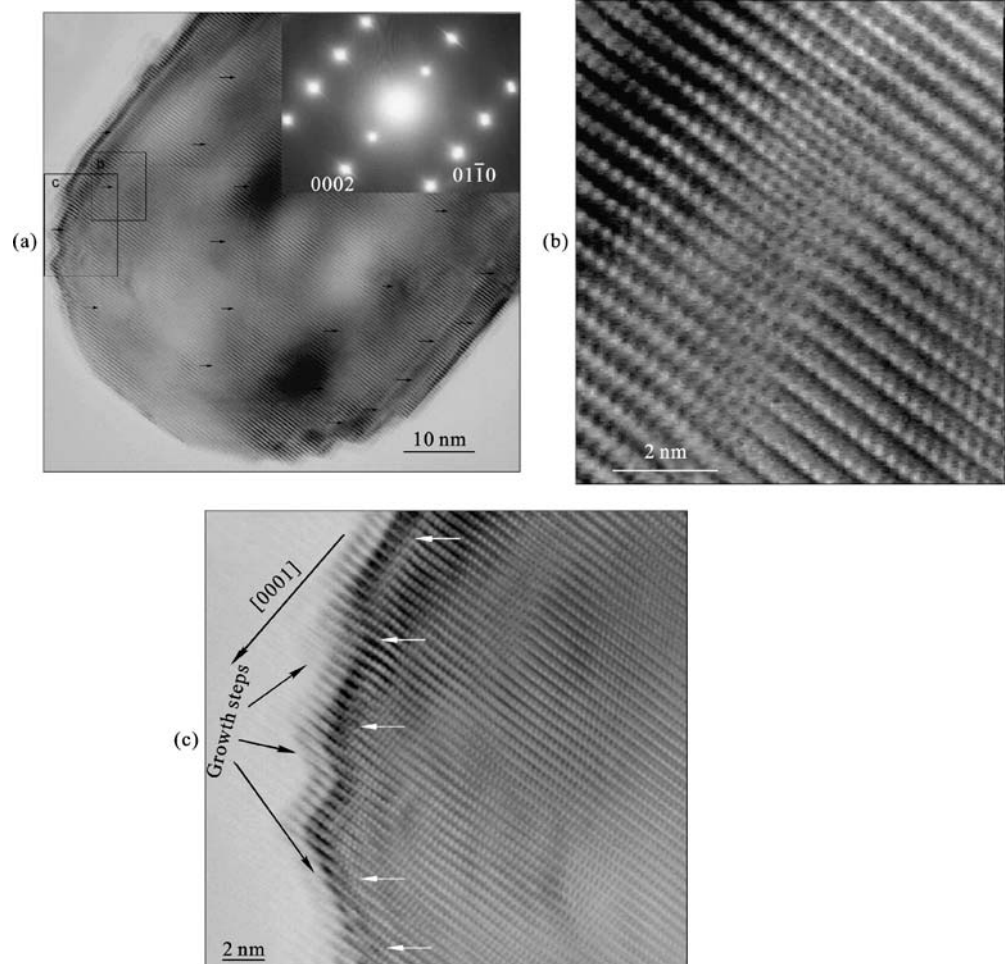


Fig. 14(a) point out some positions of the dislocations, and magnified local images are shown in Figs. 14(b) and (c). The images exhibit the periodic dislocations and the growth steps. Growth occurs around the dislocations, and the growth direction accords with the Burgers vector of the dislocations. HRTEM micrograph analysis is reliable to confirm dislocation and growth of crystals [27]. Investigations through SEM and HRTEM confirm that screw dislocation growth is one of the growth mechanisms of ZnO nanostructures.

Through investigations described above, it is revealed that VS mechanism, polar mechanism and screw dislocation growth mechanism exist in our fabrications. In other words, growth of ZnO nanostructures fabricated through pure zinc powder evaporation without a catalyst is controlled by one or combined two/three of such mechanisms.

### 3.3 Properties

#### 3.3.1 Optical properties

The PL spectrum of ZnO nanocombs [Fig. 4(c)] was measured at room temperature and is shown in Fig. 15. The excitation wavelength was 310 nm. Two typical emission peaks at  $\sim 385$  nm and  $\sim 495$  nm were observed, which were assigned to UV emission and green emission, respectively. It was reported that the improvement in crystal quality (decrease in impurities and structure defects) can result in detectable UV emission at room temperature, whereas the green transition is attributed to singly ionized oxygen vacancies in the ZnO; emission results from the radiative recombination of a photogenerated hole with an electron occupying the oxygen vacancy. The green light emission intensity increases relative to the UV emission as the wire diameter decreases, which suggests that there is a greater fraction of oxygen vacancies in the thinner nanostructures [29–31]. Therefore, it is reasonable to believe that some oxygen vacancies exist in the ZnO nanocombs and the green light emission from the ZnO nanocombs could be attributed to the single ionized oxygen vacancy.

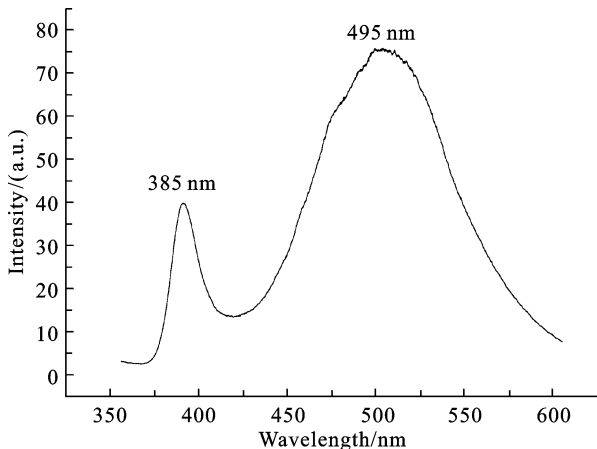


Fig. 15 PL spectrum of ZnO nanocombs at room temperature

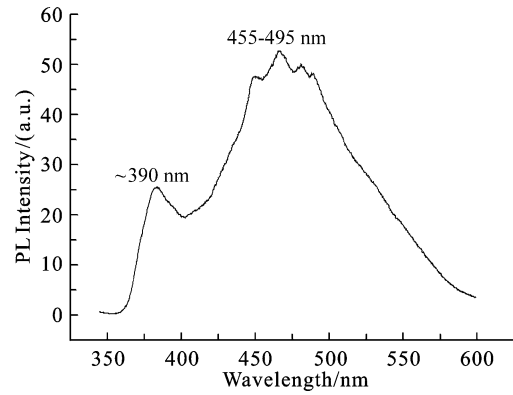


Fig. 16 PL spectrum of ZnO nanosaws II type at room temperature

Under similar experimental conditions, the PL spectrum of ZnO nanosaws II type [Fig. 4(b)] was obtained and is shown in Fig. 16 which exhibits obvious difference from Fig. 15. Two typical emission peaks at  $\sim 390$  nm and 455–495 nm were observed. But the peak at 455–495 nm includes four subordinate peaks. We consider that it is possibly related with the different type or quantity oxygen vacancies which change along with the dimensions of the backbones and the teeth of the toothed nanostructures. Wang et al. [32] reported the excursion of PL spectra of belts with different widths.

#### 3.3.2 Field emission properties

Outstanding field emission property is one of the excellent features of ZnO-based 1D nanomaterials. Many kinds of 1D ZnO nanostructures are candidates for appropriate alternative to CNT for field emission devices [33]. Field emission  $I$ - $V$  curves of ZnO nanoarrays and tetraleg nanorods were carried out by a two-parallel-plate configuration in a vacuum chamber with  $3.5 \times 10^{-7}$  Pa at room temperature. The distance between the electrodes was 300  $\mu\text{m}$ . The emission current was measured by applying a

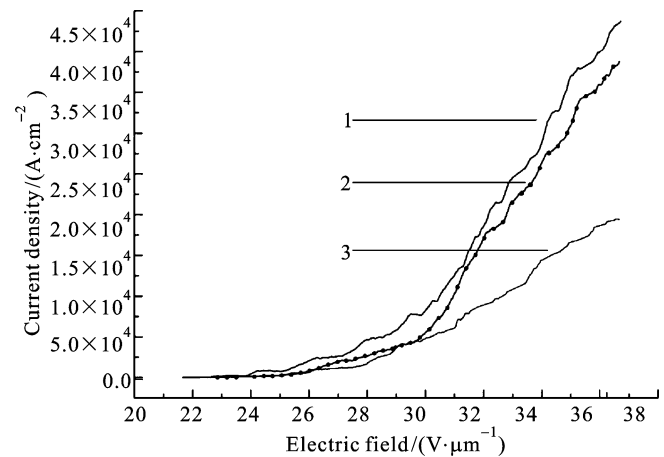
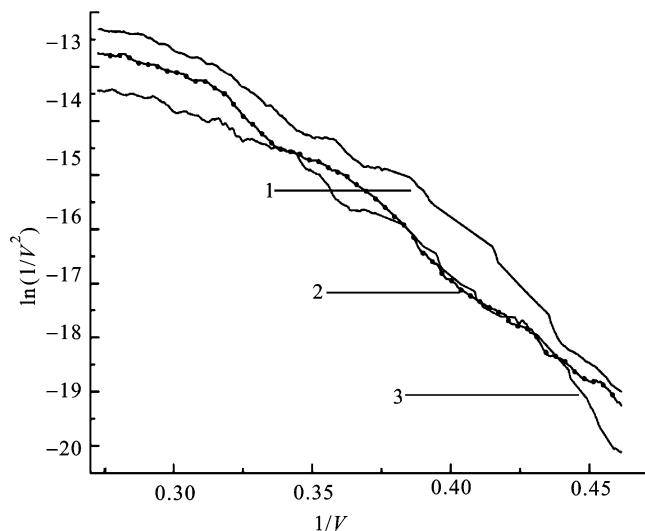


Fig. 17 Field emission  $I$ - $V$  curves from nanoarrays and tetraleg nanorods: (1) curve of nanoarrays as seen in Fig. 3(a), (2) curve of tetraleg nanorods as seen in Fig. 7(a), (3) curve of nanoarrays as seen in Fig. 3(b)



**Fig. 18** Curves of  $1/V-\ln(1/V^2)$ : (1) curve of nanoarrays as shown in Fig. 3(a); (2) curve of tetraleg nanorods as shown in Fig. 7(a); (3) curve of nanoarrays as shown in Fig. 3(b)

voltage increasing from 0.5 to 1.1 kV with a sweep step of 1 V. Results, shown in Fig. 4, demonstrated that the turn-on field of the three types of ZnO samples is about 2.3–2.4 V/ $\mu\text{m}$ , and at the field of 3.7 V/ $\mu\text{m}$ , the emission current density is  $4.31 \times 10^{-5}$ ,  $3.88 \times 10^{-5}$  and  $1.94 \times 10^{-5}$  A/ $\text{cm}^2$ , respectively. The density rises sharply as the field increases up to a certain value. In the three types of ZnO nanostructures, the emission density of nanoarrays as shown in Fig. 3(a) is the highest, whereas the density of tetraleg rods as seen in Fig. 7(a) is the secondary, and that of arrays as shown in Fig. 3(b) is the lowest. The  $I-V$  curves are shown in Fig. 17.

The electron field emission properties are usually investigated using the Fowler–Nordheim (F–N) model [33]. F–N curves [ $1/V-\ln(1/V^2)$ ] are shown in Fig. 18. It can

be seen that the curves are consistent with the F–N mechanism by exhibiting linear dependence. According to the slopes of the F–N curves (slope = 37, 36 and 32), the fields for the three types of ZnO nanostructures to reach emission current of  $10^{-3}$  A/ $\text{cm}^2$  are 4.5, 4.8 and 5.9 V/ $\mu\text{m}$ , respectively. In practice, such fields are available and such values of current density are feasible for application. The three factors, low turn-on voltage, high emission current density and good linearity of F–N curve, make ZnO 1D nanostructures, especially ZnO nanoarrays as shown in Fig. 3(a), a prospective candidate for field emission devices.

Field emission properties are markedly affected by geometry of tip and arrangement of materials. Fig. 19 shows the HRTEM images of nanoarrays as shown in Fig. 3(a). The presented image reveals that the tip is not as flat tip of arrays as shown in Fig. 3(b). The tip is a cone, or multi-edged pyramid with the apex angle of  $117^\circ$ , which accords with the angle inclined between crystallographic planes (0 $\bar{1}$ 13) and (01 $\bar{1}$ 3). Moreover, the dimension of the apex is only about 2 nm (as shown in the left-lower inset of Fig. 19), and the initial half-angle of the tip is about  $18^\circ$ . In particular, the two types of ZnO nanoarrays [as shown in Figs. 3(a),(b)] have similar distribution densities, although the measured emission current showed obvious difference. The result indicates that the geometric feature of ZnO nanorods, such as sharp apex geometry, small dimension and initial half-angle of tip, can improve the field emission property of ZnO nanorods to an outstanding level. On the other hand, that of broad and flat tops worsened the property of ZnO arrays. Results revealed that the morphology, dimension, and apex geometry of ZnO 1D nanostructures have a pronounced impact on the FE property. In addition, arrangement of materials also affects FE property. This reveals the reason why the property of tetraleg rods with similar tip geometry is lower than that of nanoarrays.

## 4 Conclusions

By controlling gas flow rates and partial pressures of argon, oxygen and zinc vapor, various types of high-quality ZnO nanomaterials (such as wires, belts, arrays, saws or combs, tetraleg rods, nails, and pins) have been successfully fabricated through pure zinc powder evaporation without a catalyst in the temperature range of 600–700°C. Deposited nanostructures were characterized via scanning electron microscopy, X-ray diffraction and high-resolution transmission electron microscopy. Growth mechanisms of various ZnO were proposed and discussed. In addition, properties of room temperature photoluminescence and field emission of several typical ZnO nanostructures were measured and investigated. Research on this field indicated that the growth of ZnO nanostructures fabricated through pure zinc powder evaporation without a catalyst is controlled by one or combined (two or three) VS mechanism, polar mechanism, or screw dislocation growth

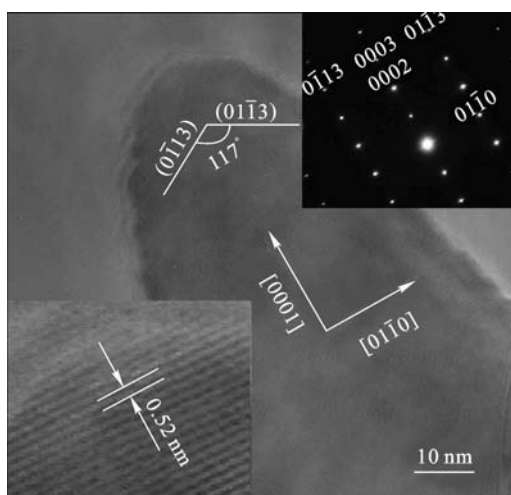


**Fig. 19** HRTEM image of a tip of ZnO nanoarrays

mechanism, and that ZnO nanostructures exhibit outstanding photoluminescence and field emission properties, although such properties can be affected by dimension, geometry and arrangement of materials.

**Acknowledgements** This study was supported by the National Science Fund for Distinguished Young Scholars (No. 50325209), the National Natural Science Foundation of China (No. 50232030 and 50572005) and the Key Project of Chinese Ministry of Education (No. 104022).

## References

- Lee C.-J., Lee T.-J., Lyu S.-C. and Zhang Y., Field emission from well-aligned zinc oxide nanowires grown at low temperature, *Appl. Phys. Lett.*, 2002, (81): 3648–3650
- Lee J.-S., Kanga M.-I., Kim S., Lee M.-S. and Lee Y.-K., Growth of zinc oxide nanowires by thermal evaporation on vicinal Si(100) substrate, *J. Cryst. Growth*, 2003 (249): 201–207
- Yuan H.-J., Xie S.-S., Liu D.-F., Yan X.-Q., Zhou Z.-P., Ci L., Wang J., J.-X., Gao Y., Song L., Liu L.-F., Zhou W.-Y. and Wang G., Characterization of zinc oxide crystal nanowires grown by thermal evaporation of ZnS powders, *Chem. Phys. Lett.*, 2003 (371): 337–341
- Huang M.-H., Mao S., Feick H., Yan H.-Q., Wu Y.-Y., Kind H., Weber E., Russo R. and Yang P.-D., Room-temperature ultraviolet nanowire nanolasers, *Science*, 2001 (292): 1897–1899
- Pan Z.-W., Dai Z. and Wang Z.-L., Nanobelts of semiconducting oxides, *Science*, 2001 (291): 1947–1949
- Dai Y., Zhang Y., Li Q.-K. and Nan C.-W., Synthesis and optical properties of tetrapod-like zinc oxide nanorods, *Chem. Phys. Lett.* 2002 (358): 83–86
- Xing Y.-J., Xi Z.-H., Zhang X.-D., Song J.-H., Wang R.-M., Xu J., Xue Z.-Q. and Yu D.-P., Nanotubular structures of zinc oxide, *Solid State Commun.* 2004 (129): 671–675
- Zhang Y., Huang, Y.-H., He J., Dai Y., Wang S. and Zhou Ch., Morphology and properties of tetraleg ZnO nanostructures fabricated by Zn-powder evaporation without catalyst at lower temperature, *Mater. Res. Soc. Symp. Proc.*, 2005 (879E): z7.7.1–6
- Huang Y.-H., Zhang Y., He J., Dai Y., Gu Y.-S., Ji Zh., Zhan X.-Y. and Zhou C., Fabrication, structures and optical property of ZnO nanobelts by a novel Zn-powder evaporation technique (in Chinese), *Acta Phys.-Chim. Sin.*, 2005 (3): 239–243
- Zhang Y., He J., Huang Y.-H., Gu Y.-S., Ji Zh. and Zhou C., Zinc powder evaporation: an efficient way of synthesizing a wide range of high-quality ZnO nanostructures at lower temperature, *Mater. Res. Soc. Symp. Proc.*, 2005 (872): J21.6.1–6
- Huang Y.-H., Zhang Y., He J., Dai Y., Gu Y.-S., Ji Z. and Zhou C., Fabrication and characterization of ZnO comb-like nanostructures, *Ceram. Int.*, in press
- Gao P.-X. and Wang Z.-L., Nanopropeller arrays of zinc oxide, *Appl. Phys. Lett.* 2004 (84): 2883–2885
- Kong X.-Y. and Wang Z.-L., Polar-surface dominated ZnO nanobelts and the electrostatic energy induced nanohelices, nanosprings, and nanospirals, *Appl. Phys. Lett.* 2004 (84): 975–977
- Kong X.-Y., Ding Y., Yang R.-S., Wang Z.-L., Single-crystal nanorings formed by epitaxial self-coiling of polar nanobelts, *Science*, 2004 (303): 1348–1351
- Dai Y., Zhang Y., Bai Y.-Q. and Wang Z.-L., Bicrystalline zinc oxide nanowires, *Chem. Phys. Lett.*, 2003 (375): 96–101
- Wang Y.-W., Zhang L.-D., Wang G.-Z., Peng X.-S., Chu Z.-Q. and Liang C.-H., Catalytic growth of semiconducting zinc oxide nanowires and their photoluminescence properties, *J. Cryst. Growth*, 2002 (234): 171–175
- Bai Z.-G., Yu D.-P., Bai Z.-G., Yu D.-P., Zhang H.-Z., Ding Y., Wang Y.-P., Gai X.-Z., Hang Q.-L., Xiong G.-C. and Feng S.-Q., Nano-scale GeO<sub>2</sub> wires synthesized by physical evaporation, *Chem. Phys. Lett.*, 1999 (303): 311–314
- Yang P.-D., Yan H.-Q., Mao S., Richard R., Justin J., Richard S., Nathan M., Johnny P., He R. and Choi H.-J., Controlled growth of ZnO nanowires and their optical properties, *Adv. Funct. Mater.*, 2002 (12): 323–331
- Yan H.-Q., He R.-R., Pham J. and Yang P.-D. Morphogenesis of one-dimensional ZnO nano- and microcrystals, *Adv. Mater.*, 2003 (15): 402–405
- Lyu S.-C., Zhang Y., Ruh, H., Lee H.-J., Shim, H.-W., Suh, E.-K. and Lee C.-J., Low temperature growth and photoluminescence of well-aligned zinc oxide nanowires, *Chem. Phys. Lett.*, 2002 (363): 134–138
- Dai Z.-R., Pan Z.-W. and Wang Z.-L., Novel nanostructures of functional oxides synthesized by thermal evaporation, *Adv. Funct. Mater.*, 2003 (13): 9–34
- Dai Y., Zhang Y. and Wang Z.-L., The octa-twin tetraleg ZnO nanostructures, *Solid State Commun.* 2003 (126): 629–633
- Lao J.-Y., Huang J.-Y., Wang D.-Z. and Ren Z.-F., ZnO nanobridges and nanonails, *Nano Lett.* 2003 (3): 235–238
- Dai Z.-R., Pan Zh.-W. and Wang Zh.-L., Novel nanostructures of functional oxides synthesized by thermal evaporation, *Adv. Funct. Mater.*, 2003 (13): 9–24
- Iwanaga H., Fujii M. and Takeuchi S., Inter-leg angles in tetrapod ZnO particles, *J. Cryst. Growth*. 1998 (183): 190–195
- Wang Z.-L., Kong X.-Y. and Zuo J.-M., induced Growth of asymmetric nanocantilever arrays on polar surfaces, *Phys. Rev. Lett.*, 2003 (91): 185502-1–3
- Hung K.-C., Lam C.-C., Li J.-Q. and Shao H.-M., Inergrowth structures and screw dislocations in Pb-doped Hg-1234 superconductor, *Physica C* 1997 (282–287): 907–908
- Dong J., Shen W., Zhang B., Liu X., Kang F., Gu J., Li D. and Chen N., New origin of spiral and new growth process of carbon whiskers, *Carbon* 2001 (39): 2325–2333
- Bagnall D.-M., Hen Y.-F.-C., Shen M.-Y., Zhu Z. and Yao T., Room temperature excitonic stimulated emission from zinc oxide epilayers grown by plasma-assisted MBE, *Cryst. Growth* 1998 (185): 605–609
- Vanheusden K., Warren W.-L., Seager C.-H., Tallant D.-R., Voigt J.-A. and Gnade B.-E., Mechanisms behind green photoluminescence in ZnO phosphor powders, *Appl. Phys.* 1996 (79): 7983–7986
- Huang M.-H., Wu Y., Feick H., Tran N., Weber E. and Yang P.-D., Catalytic growth of zinc oxide nanowires by vapor transport, *Adv. Mater.*, 2001 (13): 113–116
- Wang X., Ding Y., Summers C.-J. and Wang Z.-L., Large-scale synthesis of six-wide ZnO nanobelts, *J. Phys. Chem. B.* 2004 (108): 8773–8777
- Zhu Y.-W., Zhang H.-Z., Sun X.-C., Feng S.-Q., Xu J., Zhao Q., Xiang B., Wang R.-M. and Yu D.-P., Efficient field emission from ZnO nanoneedle arrays, *Appl. Phys. Lett.* 2003 (83): 144–146